Hindawi
Adsorption Science & Technology
Volume 2022, Article ID 5790408, 18 pages
https://doi.org/10.1155/2022/5790408

Research Article

Equilibrium and Kinetic Adsorption of Hydrogen Fluoride onto Zeolite 3A

Shuo Duan,[1] **Ke Huang**,[2] **and Mengmeng Tao**[2]

[1]*School of Mining and Geomatics Engineering, Hebei University of Engineering, Handan, Hebei 056038, China*
[2]*State Key Laboratory of Laser Interaction with Matter, Northwest Institute of Nuclear Technology, Xi'an 710024, China*

Correspondence should be addressed to Shuo Duan; duans10@sina.com

Received 15 April 2022; Revised 8 July 2022; Accepted 4 August 2022; Published 17 August 2022

Academic Editor: Stefano Salvestrini

Equilibrium and kinetic adsorption behaviours of hydrogen fluoride (HF) onto zeolite 3A were investigated under different temperatures (298–338 K) and pressures (0.15–1.1 bar). The HF adsorption isotherms on zeolite 3A were well described by the Dubinin–Astakhov (DA) model. The isosteric heat of HF adsorption was calculated based on the DA model and Clausius–Clapeyron equation, and different kinetic models were used to analyze the HF adsorption kinetic. The results showed HF adsorption isotherms are type I of the IUPAC classification. The maximum adsorption capacities by the DA model are 0.443–0.5631 mg/g. The H_{st} values decrease with increasing surface loading indicating the surface energy heterogeneity of zeolite 3A. The HF adsorption kinetics on zeolite 3A follows simple first-order kinetics. The calculated film diffusion parameter B_t values show nonlinear characteristics with time. The order of magnitude of interparticle HF diffusion coefficient D_c is 10^{-9} m^2/s. The higher pressure and temperature are in favour of HF diffusion. The intraparticle diffusion curves for HF adsorption on zeolite 3A show quart-linear characteristics, indicating the presence of four consecutive HF adsorption steps including film diffusion, interparticle diffusion, intraparticle diffusion, and surface adsorption. The intraparticle diffusion is a rate-controlling stage.

1. Introduction

Fluorine-containing chemicals are widely used in atomic energy, metallurgy, machinery, chemical industry, and other industries because of their unique physical and chemical characteristics [1]. As a basic fluorine chemical product, hydrogen fluoride (HF) is widely used in producing refrigerants, fluorine resin, fluorine rubber, and fluorine-containing intermediate and fine chemicals [2]. HF is corrosive and toxic, and it poisons humans and animals through the food chain, destroys the normal metabolism of calcium and phosphorus, inhibits enzyme activity, and affects the nervous system [1]. In the use of fluorine (F_2), e.g., uranium enrichment, optics, and material fluorination, HF is often accompanied by F_2, which reduces the purity of fluorine [3–5]. Therefore, HF purification treatment and recovery are indispensable to save resources and protect the environment.

The common methods of collecting and recovering HF are compression condensation, absorption, and adsorption [6]. The compression condensation method can purify HF gas well in theory, but this method needs low temperature and consumes more energy [7]. The HF amount treated by the absorption method is huge. However, absorption purification is wet with high requirements for equipment and chemical treatment problems [8]. Collecting HF by adsorption method cannot only remove HF gas but also reduce the emission of toxic gas HF and energy consumption. The adsorption method is mainly based on the HF adsorption performance. Thus, the basic HF adsorption data is required [9]. The frequently used adsorbents for HF adsorption are porous, e.g., sodium fluoride, activated alumina, activated carbon, and silica gel [2]. Zeolite is a commonly used adsorption material in gas separation and gas purification [6]. The application of zeolite can be extended to HF treatment.

The studies on HF treatment by adsorption have been investigated by some scholars. Sodium fluoride (NaF) is a commonly used adsorption material for HF [10–12]. NaF reacts with HF to produce $NaHF_2$. When the temperature is higher than 250°C, $NaHF_2$ can be decomposed into NaF and HF. Afzal et al. conducted experiments on HF adsorption with NaF by the fixed bed, and the influence of

concentration, temperature, and other parameters on the surface loading has been studied in detail [10–12]. The experimental results show that Langmuir and Temkin can better describe the HF adsorption isotherm than Freundlich [11]. Moreover, Liu et al. used NaF to adsorb and remove trace HF in the production of high-purity tungsten hexafluoride, and the HF adsorption by NaF under different temperatures, pressures, and gas flows was measured by orthogonal test [13]. The results showed the suitable adsorption temperature was 20–80°C, and the flow rate has a significant effect on adsorption efficiency. Activated alumina (Al_2O_3) is also used for HF adsorption. Activated alumina reacts with HF to produce AlF_3 and H_2O. In addition, Wu et al. studied the adsorption characteristics and influencing factors for HF adsorption by Al_2O_3, and the relationships between crystal structure, the specific surface area of Al_2O_3, and HF adsorption have been considered [14]. Sheng studied the HF adsorption behaviour on activated carbon, calcium oxide, activated alumina, iron oxide, and fly ash, and the Freundlich model described the adsorption isotherms well [15]. In addition to NaF and Al_2O_3, some other porous materials are also gradually applied to HF adsorption. Che et al. studied the HF adsorption behaviour on DB18C6/SiO2 composite [16]. Siahooe et al. studied the HF adsorption on carbon nanotubes and found that the HF adsorption density decreased with temperature increase [17]. Wang et al. investigated the HF adsorption behaviour on three metal–organic frameworks (MOFs) and found that MOFs had better HF adsorption performance than commercial Al_2O_3 and 13X zeolite [18]. Bahrami et al. investigated the HF gas adsorption by three kinds of activated carbon under vacuum and described the experimental data by isotherm adsorption models [19].

Zeolite 3A is an excellent performance adsorbent for gas storage and separation [20]. However, the studies about HF adsorption on zeolite 3A are very lacking. Therefore, the study of the adsorption characteristics and influencing factors of HF on zeolite 3A is necessary. In this study, the equilibrium and kinetic adsorption curves of HF on zeolite 3A at different temperatures and pressures were measured. The HF adsorption isotherms on zeolite 3A were described by the three isotherms model. The DA model and the Clausius–Clapeyron equation were used to calculate the isosteric heat of HF adsorption, and different kinetic models were used to analyze the kinetic process for HF adsorption on zeolite 3A. The adsorption mechanism of HF onto zeolite 3A was evaluated based on kinetics and thermodynamics.

2. Materials and Methods

2.1. Materials. Zeolite 3A ($8(K_{12}[(AlO_2)_{12}(SiO_2)_{12}]\cdot 24H_2O)$ used in this study was commercial zeolite manufactured by Lu Xinyuan Company (Henan, China). In this investigation, spherical 3A particles of 0.2 cm radius were studied. Hydrogen fluoride and helium with a purity of 99.99% were provided by China Shipbuilding (Handan) Perry Special Gas Co., Ltd.

2.2. Characterization of the Zeolite 3A. The compositions were measured by X-ray diffraction (XRD) using a Rigaku Smartlab 9kW with Cu Kα radiation (40 kV and 40 mA). The Fourier transform-infrared (FT-IR) of zeolite 3A spectra was obtained from an FT-IR spectrometer (Thermo Nicolet iS5, USA) using pellets of zeolite/KBr. The surface morphology was obtained by SEM (Zeiss sigma500) at an accelerating voltage of 10 kV. The pore structure distribution (PSD) of zeolite 3A was measured by the low-temperature CO_2 adsorption method at 273 K using 3H-2000 PM.

2.3. Adsorption Isotherm and Kinetics Measurements. Equilibrium and kinetics measurements of HF adsorption on zeolite 3A were performed in a static volumetric instrument. The detailed composition of the experimental instrument is shown in Figure 1. The pressures of the experimental system were recorded using a precision pressure sensor (Keller, Switzerland, ±0.01% precision). An automatic thermostatic oil bath with ±0.01 K accuracy was used to keep the system temperature constant.

The main experimental procedures for equilibria and kinetics adsorption are:

(1) Sample pretreatment and filling. The 3A sample used in the adsorption experiment was first dried in the drying oven at 385 K for 24 h, weighed, and then quickly transferred to the sample cell. The constant temperature of the oil bath was set to 358 K and vacuumed for 12 h to remove the water and other impurities adsorbed in the sample transfer process

(2) Leakage test for adsorption system. After the sample pretreatment, the temperature of the oil bath was set to 338 K. After the system temperature is constant, helium (He) was fed into the reference and adsorption cells to a certain value (maximum pressure required for adsorption). The leakage testing time was 12 h. The system was heated and vacuumed for 4 h after the leakage test

(3) Measurement of void volume. The void volume of the adsorption cell filled with adsorbent was measured by the helium expansion method. The temperature for the helium expansion test was set to the adsorption experimental temperature. The helium density used in void volume measurement is calculated by the BWR equation [21]. Helium expansion tests were repeated at least four times and the values were averaged to minimize error

(4) Equilibrium adsorption experiment. A certain HF amount was injected into the reference cell when the temperature of the adsorption system was constant with the experimental setting value. The gas pressure for the reference cell was recorded until it is stable. The valve between the reference and sample cells was opened, the HF flowed into the sample cell from the reference cell and the adsorption began. The system pressure was recorded when the system pressure was constant for 5 h. The above operations were repeated until the maximum pressure point of the equilibrium adsorption is reached

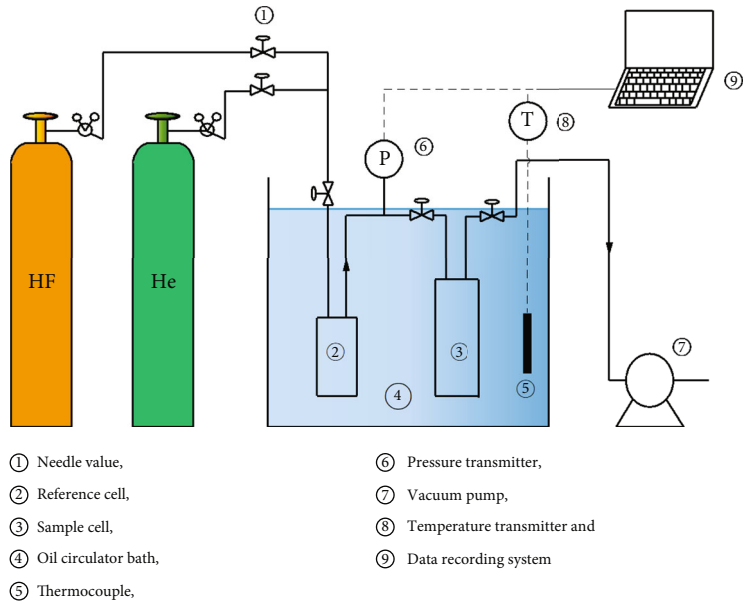

Figure 1: A schematic of experimental setup for HF adsorption.

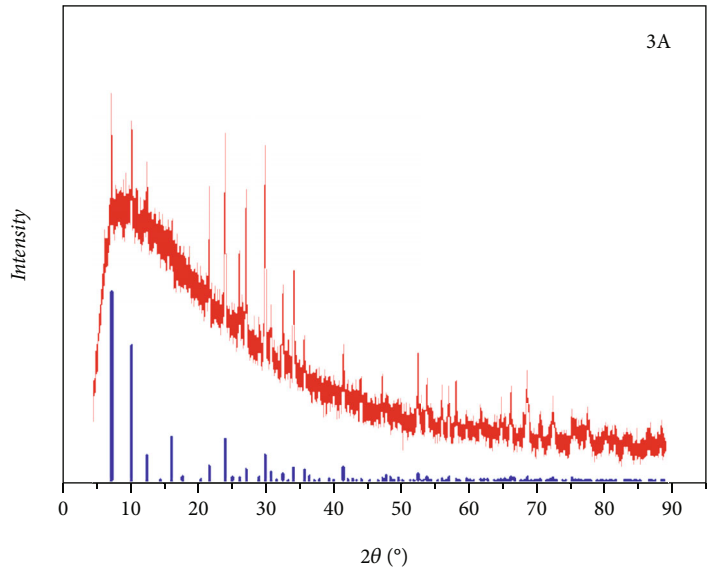

Figure 2: XRD pattern of zeolite 3A.

(5) Adsorption kinetics experiment. HF was injected into the reference cell to a calculated pressure value when the temperature of the adsorption system was constant with the experimental set value. The valve between the reference and sample cells was then opened, the HF flowed into the adsorption cell, and the system pressure was recorded in real time by the high-precision pressure transmitter until the final system pressure was stabilized at the desired value. The kinetic experimental conditions were 0.15, 0.35, 0.5, 0.70, 0.95, and 1.10 bar at 298 K and 298, 308, 318, 328, and 338 K at 0.5 bar

During the experiment, the calculation process for HF adsorption capacity was based on the mass conservation under the ideal gas state, so the adsorption capacity is [19]:

$$q = \frac{1}{RT}\left[p^0 V_R - p^1 (V_R + V_v)\right], \quad (1)$$

where q is the adsorption capacity, p^0 is the gas pressure in the reference cell before adsorption and p^1 is the system gas pressure during the adsorption process. R and T are the ideal gas constant and the system temperature, respectively.

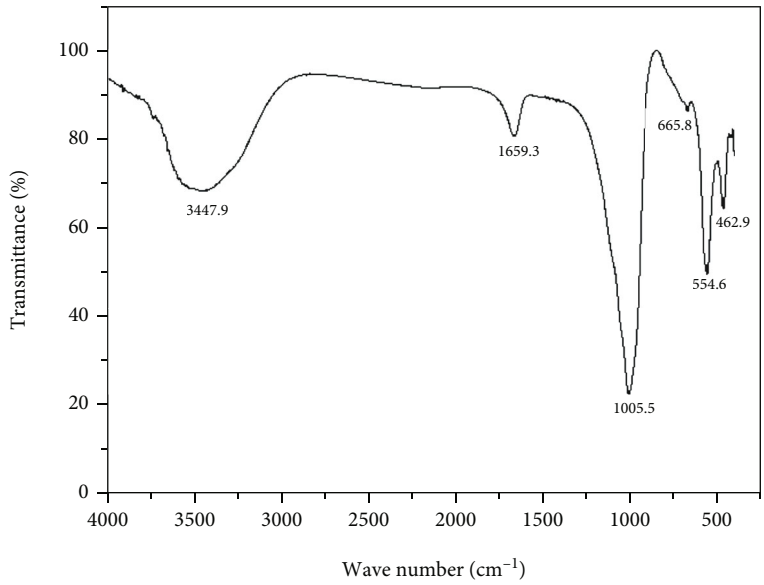

Figure 3: IR spectra of zeolite 3A.

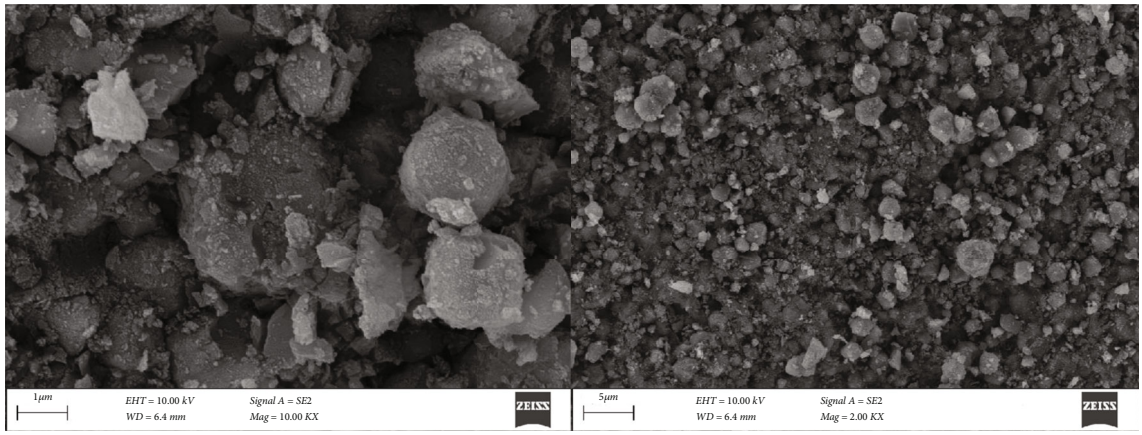

Figure 4: SEM images of zeolite 3A.

2.4. Adsorption Theory

2.4.1. Isotherm Models. The relationship between adsorption capacity, temperature, and pressure in the adsorption process is usually described by the adsorption model. The Langmuir and Freundlich models had been successful in adapting the described HF adsorption process [11, 12]. The DA model is often used to describe the gas adsorption in micropores [22]. The DA model is expressed as follows:

$$q = q_m \exp\left(-\left(\frac{RT}{E}\ln\left(\frac{p_0}{p}\right)\right)^n\right), \quad (2)$$

where q and q_m are the adsorption capacity and saturated adsorption capacity of gas, p_0 is the saturated vapor pressure of gas, and E is the adsorption characteristic energy.

The saturated vapor pressure p_0 of HF is calculated by the Antoine equation with extension [23]:

$$\log_{10} p_0 = A + \frac{B}{T} + C\log_{10} T + DT + ET^2, \quad (3)$$

where the values of A, B, C, D, and E are 23.7347, −1799.6, −6.1764, 5.0046×10^{-10}, and 6.15×10^{-6}, respectively. The unit of p_0 is mmHg in the calculation formula, which needs to be multiplied by 0.0013332 to convert to bar. The calculated saturated vapor pressures of 298, 308, 318, 328, and 338 K are 1.215, 1.678, 2.223, 3.130, and 4.149 bar, respectively.

2.4.2. Heat of Adsorption. The isosteric heat of adsorption is an important thermodynamic parameter which indicates that heat released since the adsorbed state is more stable

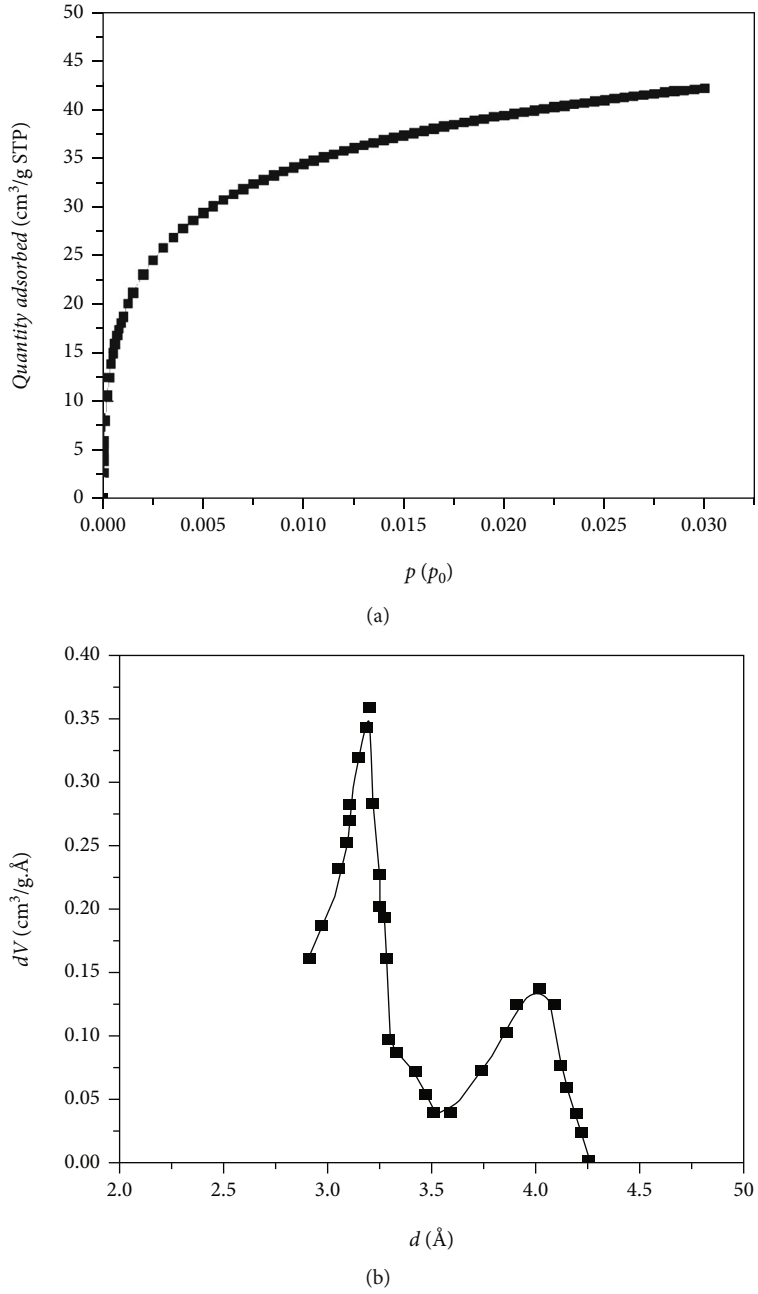

FIGURE 5: (a) Low-temperature CO_2 isotherm. (b) PSD of zeolite 3A.

than the unadsorbed state for adsorbate molecule [24]. The Clausius–Clapeyron equation was used to calculate the isosteric heat at constant adsorption capacity, and its expression is as follows [24]:

$$H_{st} = -R \left. \frac{\partial \ln p}{\partial (1/T)} \right|_q, \tag{4}$$

where H_{st} is the calculated isosteric heat at the adsorption capacity q.

The isosteric heat of adsorption (H_{st}) can be obtained by combining the DA model with the Clausius–Clapeyron equation [24]:

$$H_{st} = E\left[(-\ln \theta)^{1/n} + \frac{\alpha T}{n}(-\ln \theta)^{1-n/n}\right] + h_{fg}, \tag{5}$$

where α is the thermal expansion coefficient of adsorbed phase and α is calculated by $1/T$. h_{fg} is the enthalpy of evaporation, which is expressed as follows:

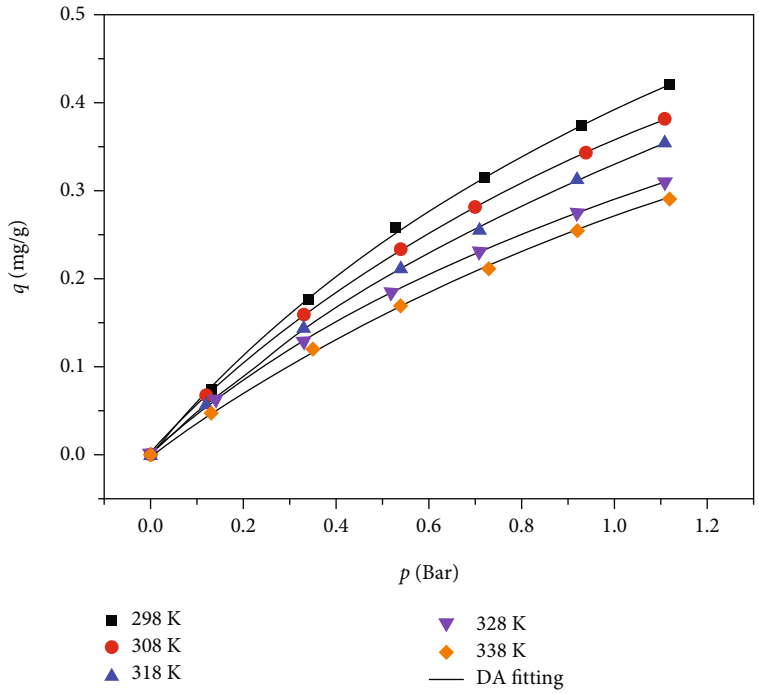

Figure 6: Adsorption isotherm and DA fitting of HF on zeolite 3A.

$$h_{fg} = -R \frac{\partial \ln p_0}{\partial (1/T)}\bigg|_C. \quad (6)$$

2.4.3. Adsorption Kinetics

(1) Adsorption Rate Models. The pseudo first-order (PFO) model assumes that the adsorption rate is directly proportional to the number of active sites. The rate expression is given by [25, 26]:

$$dq/dt = k_1(q_1 - q), \quad (7)$$

where q_1 and q represent the adsorption capacity at equilibrium and time t, respectively, and k_1 is the first-order rate constant.

After integrating Eq. (7) with the boundary conditions (t =0, q =0 and $t = t_\infty$, $q = q_1$),

$$q = q_1\left(1 - e^{-k_1 t}\right). \quad (8)$$

The pseudo second-order model (PSO) assumes the adsorption rate is proportional to the square of number of active sites; therefore, the rate model is given by [25, 26]:

$$dq/dt = k_2(q_2 - q)^2, \quad (9)$$

where q_2 represents the equilibrium adsorption capacity, and k_2 is the second-order rate constant.

With the boundary conditions (t =0, q =0 and $t = t_\infty$, q $= q_2$), the PSO is given by [25, 26]:

$$q = k_2 q_2^2 t/(1 + k_2 q_2 t). \quad (10)$$

(2) Diffusion Models.

(1) Film diffusion

Boyd's film diffusion model assumes that the main diffusion resistance is boundary film around the adsorbent particles [26, 27]. Therefore, the model was used to distinguish whether the film diffusion was a rate-controlling step in HF adsorption on 3A. The expression of this model is given by [26]:

$$F = 1 - \frac{6}{\pi^2}\sum_{n=1}^{\infty}\frac{1}{n^2}\exp\left(-n^2 B_t\right), \quad (11)$$

where F is the fraction at times t and can be expressed using adsorption capacity:

$$F = \frac{q_t}{q_m}. \quad (12)$$

B_t can be expressed in F [28]:
when $F > 0.85$,

$$B_t = -0.4977 - \ln(1 - F), \quad (13)$$

Table 1: Fitting results of the studied isotherm model.

Model	Fitting parameters	Temperature (K)				
		298	308	318	328	338
Langmuir	q_0/mg·g^{-1}	1.027	0.988	0.921	0.875	0.827
	b_L/bar^{-1}	0.618	0.571	0.554	0.505	0.481
	$SSE/\times10^{-5}$	3.753	4.301	3.862	4.153	3.922
	$RMSE$/%	0.367	0.435	0.374	0.432	0.389
	χ^2/%	0.015	0.027	0.022	0.019	0.023
Freundlich	k_F/mg·g^{-1}	0.394	0.359	0.331	0.292	0.270
	n	1.360	1.368	1.302	1.373	1.271
	$SSE/\times10^{-5}$	4.273	4.681	4.381	4.872	4.396
	$RMSE$/%	0.374	0.424	0.395	0.433	0.416
	χ^2/%	0.017	0.024	0.023	0.020	0.021
DA	q_m/mg·g^{-1}	0.4330	0.4913	0.5236	0.5452	0.5631
	E /J·mol^{-1}	3472.04	3753.22	4146.69	4523.53	5005.89
	n	1.1926	1.2186	1.2423	1.2947	1.3568
	$SSE/\times10^{-5}$	3.085	2.723	2.951	2.843	3.021
	$RMSE$/%	0.306	0.355	0.393	0.347	0.316
	χ^2/%	0.014	0.017	0.016	0.014	0.014

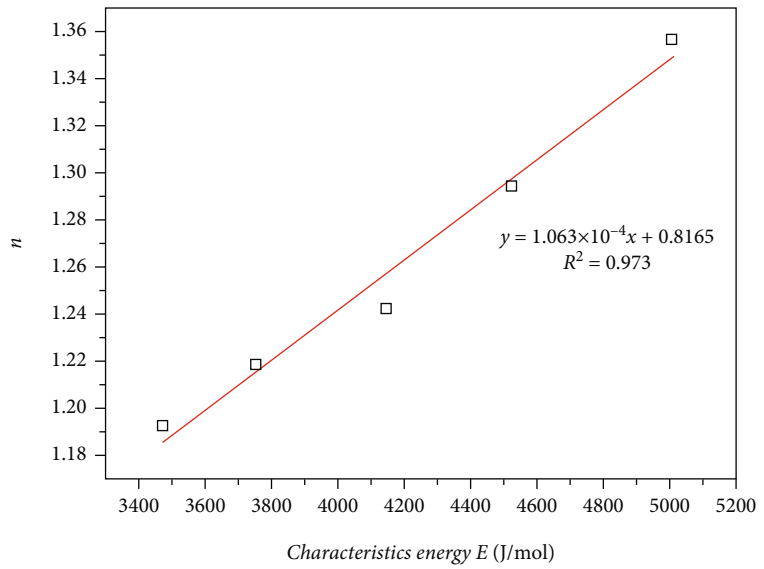

Figure 7: Linear relationship between DA parameter n and E.

when $F < 0.85$,

$$B_t = \left(\sqrt{\pi} - \sqrt{\pi - \left(\frac{\pi^2 F}{3}\right)}\right)^2. \quad (14)$$

(2) Interparticle diffusion

The model assumes interparticle diffusion control the adsorption rate, the model is given by the following expression [26, 27]:

$$\frac{q_t}{q_e} = 1 - \frac{6}{\pi^2}\sum_{n=1}^{\infty}\frac{1}{n^2}\exp\left(-\frac{n^2\pi^2 D_c t}{r_p^2}\right), \quad (15)$$

where q_t is adsorption amount at time t, q_e is adsorption amount at infinite time, D_c is interparticle diffusion coefficient, and r_p is the radius of the particle. When q_t/q_e value is >70%, Eq. (15) can be simplified to [26]:

$$\frac{q_t}{q_e} = 1 - \frac{6}{\pi^2}\exp\left(-\frac{\pi^2 D_c t}{r_p^2}\right). \quad (16)$$

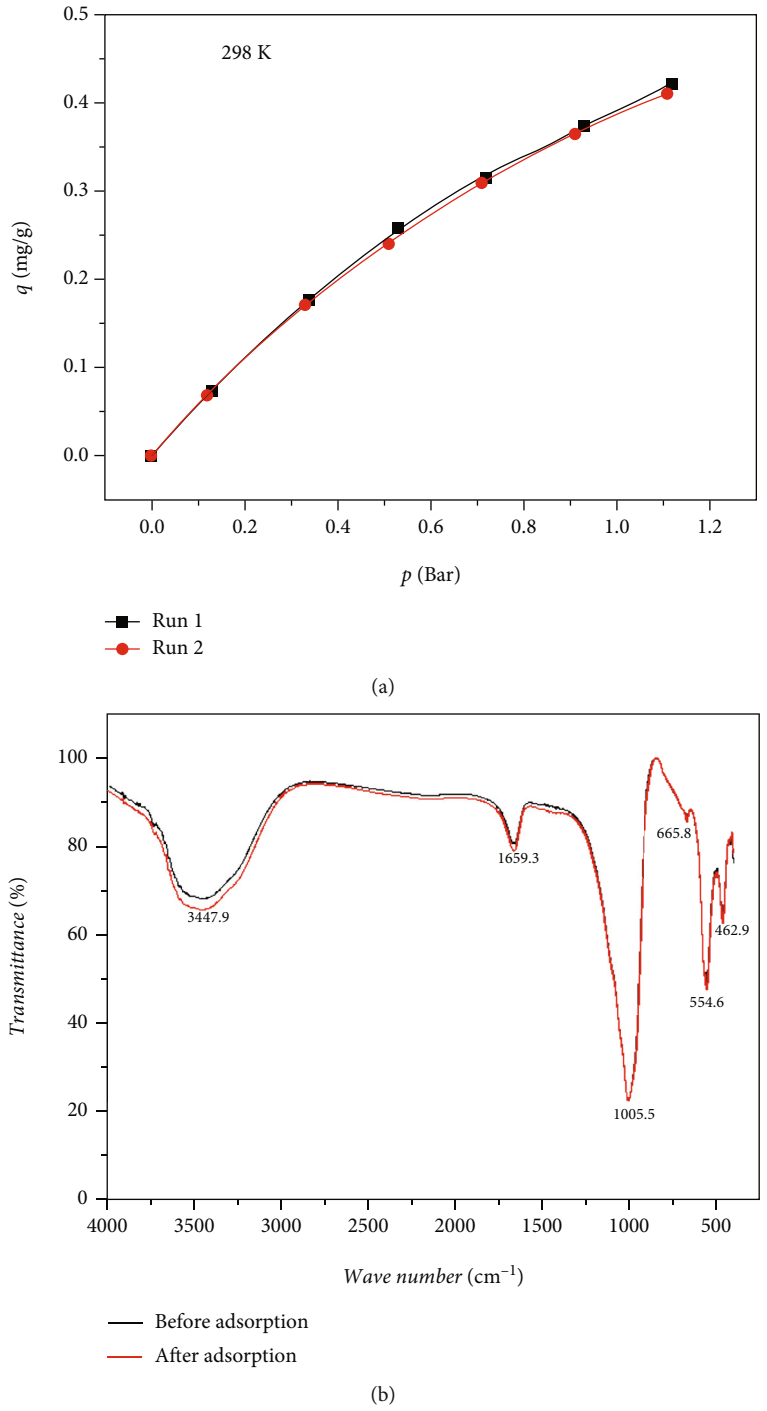

Figure 8: (a) Repeatability experiments of HF on zeolite 3A at 298 K. (b) IR spectra of the zeolite 3A before and after HF adsorption.

By plotting $\ln[1 - q_t/q_e]$ versus t, the linear slope is $-\pi^2(D_c/r^2{}_p)$ and the intercept is $\ln 6/\pi^2$.

(3) Intraparticle diffusion

If the HF adsorption process on zeolite 3A is controlled by intraparticle diffusion, the HF adsorption (q_t) should change linearly with time square root ($t^{1/2}$) [26, 27]. The intraparticle diffusion model assumes three steps typically in adsorption: bulk or film diffusion, gradual adsorption, and the final adsorption equilibrium [26]. The intraparticle diffusion model can be used for determining the adsorption mechanism, and the model is given by [29]:

$$q_t = k_i t^{1/2} + C, \tag{17}$$

where k_i is the intraparticle diffusion constant and C is the intercept. The intercept value is related to the film

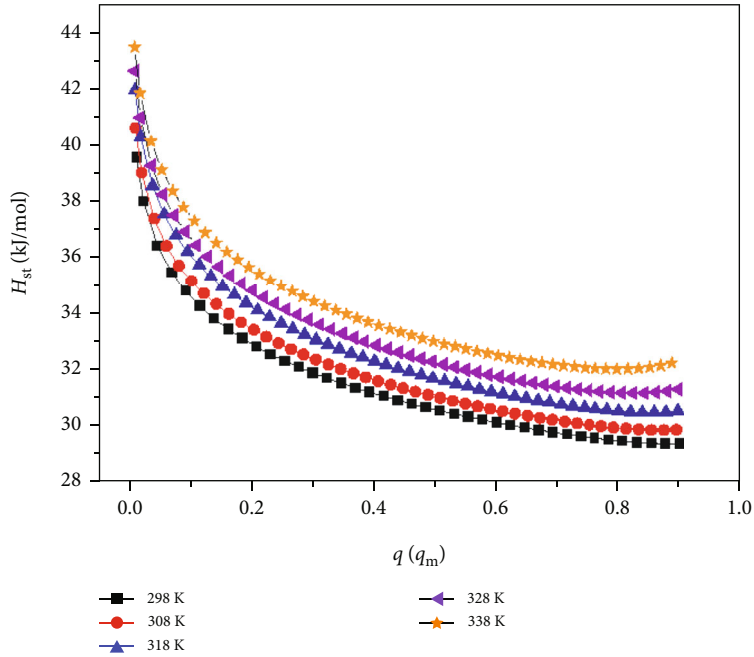

FIGURE 9: The isosteric heat of adsorption (H_{st}) of HF.

thickness. A large intercept value suggests a great film effect.

3. Results and Discussion

3.1. Characterizations of the Zeolite 3A. The powder XRD pattern of zeolite 3A is shown in Figure 2. The XRD characteristic diffraction peaks are in accordance with 3A crystals by Wang [30], indicating that the sample is a typical 3A zeolite. The FT-IR of zeolite 3A spectra is shown in Figure 3. The broad bands around 3,447.9 cm^{-1} belong to the stretching vibration of the O-H group. The bands at around 1,659.3 cm^{-1} belong to the bending and tensile vibrations of the O-H and Si-OH groups, respectively [31]. At about 1,005.5, 665.8, and 462.9 cm^{-1}, three typical absorption peaks formed by amorphous aluminosilicate structure were observed, which belong to the asymmetric tensile vibration of the tetrahedron in the sample, the symmetric tensile vibration of the Si-O-Si bond, and the bending vibration of T-O (T is Si or Al) bond, respectively [31]. The same absorption peaks have also been found by Cao et al. [31]. The absorption peak at 554.6 cm^{-1} belongs to the vibration of double binary ring D4R, the main subunit structure unit of zeolite 3A.

The surface morphology of zeolite 3A is shown in Figure 4, which indicates that the surfaces of the samples are not homogeneous. Zeolite 3A has a large grain size, good dispersibility, and many surface fractures, which has also been found in the literature [30]. The low-temperature CO_2 isotherm and PSD of zeolite 3A are shown in Figure 5. The pore size of zeolite 3A is mainly concentrated at ~0.3 and 0.37 nm. The specific surface area of zeolite 3A and the pore volume are 402.81 m^2/g and 0.1325 cm^3/g, respectively.

3.2. Adsorption Equilibrium

3.2.1. Adsorption Isotherms. The HF adsorption isotherms on zeolite 3A at 298 to 338 K are shown in Figure 6. All adsorption isotherms are type I according to the IUPAC classification. The adsorption amount of HF on zeolite 3A is close to that on activated carbon by Shen et al. [15] but less than that on activated carbon by Bahrami et al. [19] and MOF [18], which is mainly due to the pore characteristics and surface physicochemical properties of the adsorbent. The adsorption capacity increases with increasing pressure at the same temperature. The adsorption capacity decreases with the temperature increase because the binding strength of the zeolite 3A surface decreases with temperature, indicating that the HF adsorption on the zeolite 3A surface is exothermic. The Langmuir, Freundlich, and DA models were used to correlate the HF adsorption data using regression analysis [19]. Three statistical functions, including SSE, RMSE, and χ^2, were used to estimate the goodness of fit [24].

The fitting parameter values for the three models are listed in Table 1. The Langmuir parameters q_0 and b_L all decreased with the increasing temperature, which implied that the bonding of HF to zeolite decreased. The Freundlich parameter k_F represents the adsorption capacity, and n shows the adsorption driving force and indicates the favourability of adsorption [10]. The k_F values showed a negative correlation with temperature. The n values (1.271–1.368), determined from the Freundlich model suggested the moderately difficult nature of HF adsorption on zeolite 3A [10]. The same results for the Freundlich parameter n have been found in HF adsorption on produced NaF pellets and activated carbon [10–12].

The values of SSE, RMSE, and χ^2 in Table 1 for the DA model are the smallest among the three adsorption models,

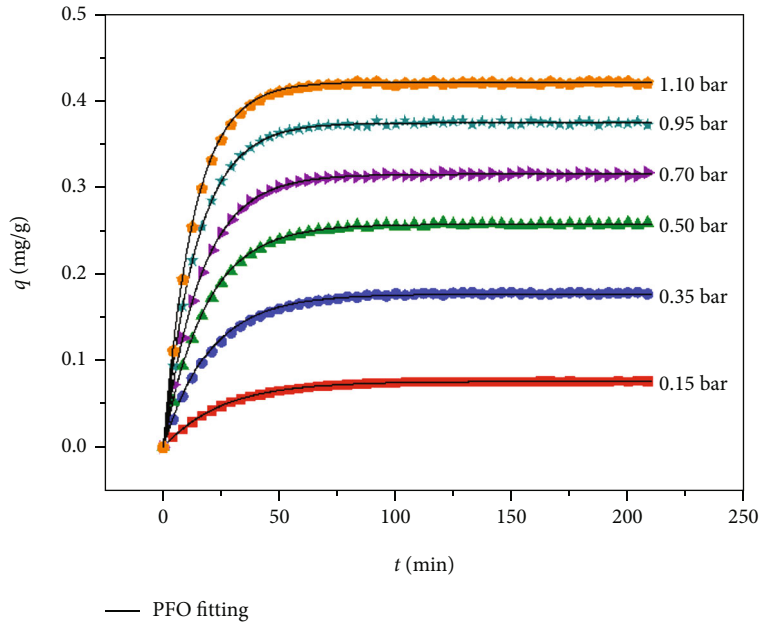

Figure 10: Dynamic curves of HF under different pressures at 298 K.

which indicates that the DA model predicted the adsorption data better than the other models. Figure 6 also shows the predicted HF adsorption data by the DA model. The DA model can describe well the HF adsorption curve, indicating that micropore filling existed in HF adsorption on zeolite 3A. Both characteristic energy E and DA parameter n increased with the increase of temperature. The DA parameter n can be used to describe the surface heterogeneity of the adsorbent [13, 24]. The study shows that the closer the n value is to 1, the higher the heterogeneity of the zeolite 3A surface, which is more related to the active adsorption site at low temperatures. The n value shows a positive correlation with the characteristics energy value E (Figure 7). The lower n value results in E value.

The regeneration of 3A zeolite affects the reuse of materials [18]. The adsorption capacity after regeneration was tested at 298 K. The zeolite 3A after HF adsorption was treated at 393 K in the muffle furnace for 12 h and then quickly transferred and sealed to the adsorption equipment (sample cell in Figure 5) and then vacuumed at 373 K for 10 h to reactivate its capacity. The HF repeatability experiments on zeolite 3A at 298 K are shown in Figure 8(a). The remaining HF capacity after regeneration was slightly reduced, which suggested the high stability of exposure to dry HF gas. The IR spectra of the zeolite 3A before and after HF adsorption are shown in Figure 8(b), suggesting no change in the surface functional group of the zeolite 3A molecular sieve after HF adsorption.

3.2.2. Heat of Adsorption. The isosteric heat of adsorption (H_{st}) calculated using Eq. (5) is plotted with the HF surface load (q/q_m), as shown in Figure 9. H_{st} values of HF on zeolite 3A decrease with the increase of surface loading, which indicates the surface energy heterogeneity of zeolite 3A. A large number of vacant adsorption sites exist on the zeolite 3A surface at the initial stage, which results in strong interaction between the HF molecules and zeolite 3A. Therefore, the H_{st} value is high at the initial adsorption stage. With further adsorption capacity increase, the adsorption sites are occupied, resulting in the weakening of the interaction between the HF molecules and zeolite 3A. Therefore, H_{st} decreases with the surface loading.

Table 2: The fitting kinetic parameters for PFO and PSO.

Pressure (bar)	Pseudo first-order			Pseudo second-order		
	q_1 /mg·g^{-1}	k_1 /min^{-1}	R^2	q_2 /mg·g^{-1}	k_2/g mg^{-1}·Min^{-1}	R^2
0.15	0.0744	0.0395	0.9999	0.0844	0.6352	0.9783
0.35	0.1768	0.0472	0.9998	0.1966	0.3485	0.9726
0.50	0.2580	0.0534	0.9998	0.2832	0.2859	0.9685
0.70	0.3153	0.0616	0.9997	0.3426	0.2863	0.9638
0.95	0.3746	0.0687	0.9998	0.4037	0.2806	0.9602
1.10	0.4206	0.0743	0.9997	0.4510	0.2775	0.9576

3.3. Adsorption Kinetics

3.3.1. Effect of Pressure on Adsorption Kinetic. The adsorption kinetic curve of HF on zeolite 3A at 298 K is shown in Figure 10. The adsorption capacity continuously increases with the adsorption time. The adsorption capacity rapidly increases in the initial stage, which is mainly due to the high adsorption energy sites on the adsorbent surface and the rapid occupation of HF molecules onto the adsorption sites, so the adsorption rate is high. When large numbers of active adsorption sites are occupied, the adsorption sites available for HF molecules become less; hence, the adsorption rate becomes slow. When the active sites are almost occupied,

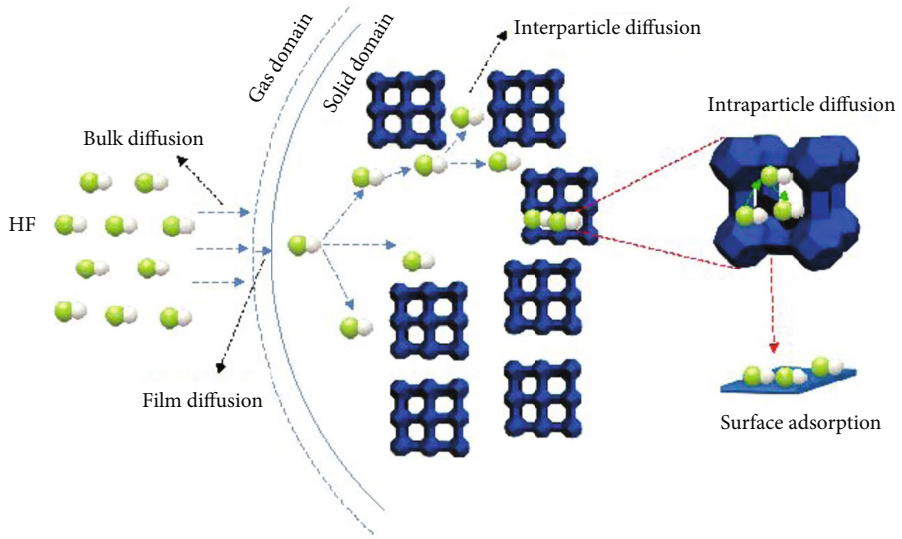

Figure 11: Adsorption mechanism of HF on 3A zeolite.

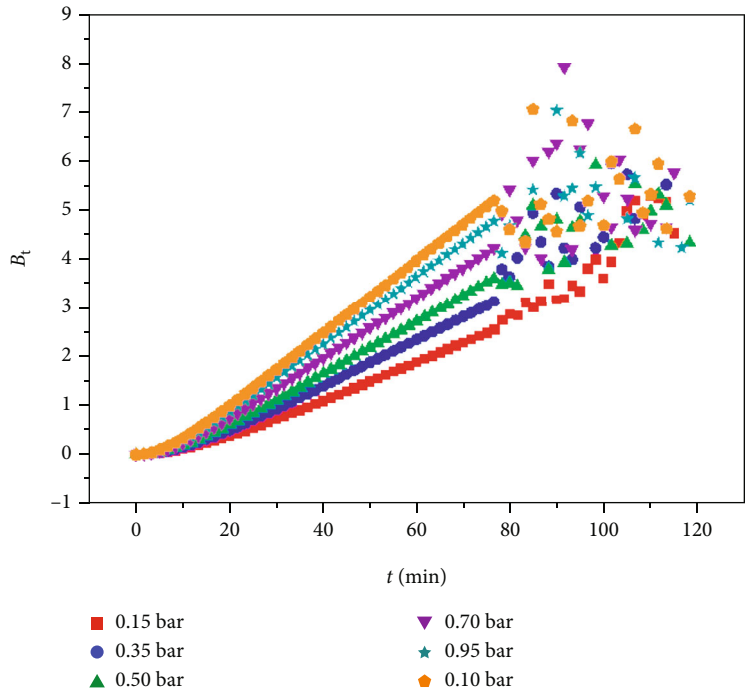

Figure 12: Plots of Boyd's film model for HF adsorption on 3A.

Table 3: Kinetic parameters of linear fitting of film diffusion model.

Pressure (bar)	Slope	Intercept	R^2
0.15	0.03954	−0.42992	0.99765
0.35	0.04693	−0.42781	0.99872
0.50	0.05256	−0.40566	0.99926
0.70	0.06069	−0.40949	0.99933
0.95	0.0678	−0.41098	0.99936
1.10	0.07321	−0.41012	0.99936

HF molecules reach dynamic equilibrium on the surface of zeolite 3A. At this time, the number of HF molecules on the adsorbent surface will not increase; therefore, the total adsorption rate tends to zero and the adsorption capacity will not increase.

(1) Adsorption Rate. The HF adsorption kinetics curves and the corresponding curves predicted by the PFO model are shown in Figure 10. The kinetic constants calculated with the PFO and PSO models and the characteristic parameters of the kinetic model are listed in Table 2. The larger R^2 of the

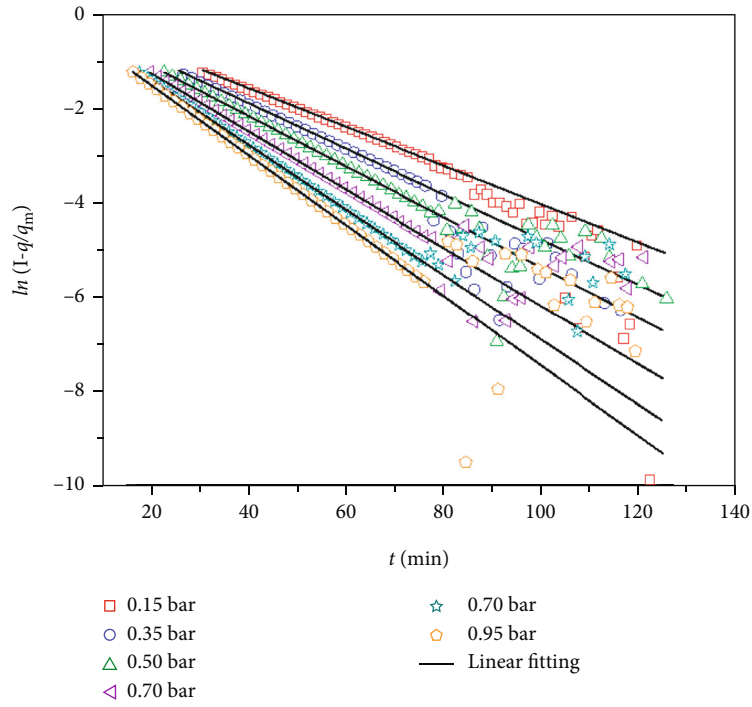

Figure 13: Linear fitting for experimental data with interparticle diffusion model.

Table 4: The linear fitting results for interparticle diffusion model.

Pressure (bar)	Slope	Intercept	D_c/r^2_p (10^{-3} s^{-1})	D_c (10^{-9} s^{-1})
0.15	−0.04085	0.09071	4.143	1.036
0.35	−0.04809	0.06103	4.877	1.219
0.50	−0.05338	0.00001	5.414	1.354
0.70	−0.06156	0.00003	6.244	1.561
0.95	−0.06873	0.00003	6.971	1.743
1.10	−0.07424	0.00002	7.530	1.882

PFO model indicates a better predictivity of the adsorption kinetic process over the whole pressure range well, so the adsorption of HF by zeolite 3A follows simple first-order kinetics. The calculated q_1 values from the PFO model are more in accordance with the experimental data than the calculated q_2 values by the PSO model.

Both q_1 and q_2 increase with pressure, which is consistent with the high pressure is conducive to HF adsorption. Meanwhile, the PFO and PSO model parameters (k_1 and k_2) increase with pressure because the velocity of the HF molecule will increase and the migration speed of HF molecules inside the pores will be faster at higher pressure, leading to an increase in the diffusion rate. The increased mass transfer coefficient makes the kinetic curve steeper. The k_1 values (0.0395–0.0743 min^{-1}) for HF on zeolite 3A are larger than that of H_2S (0.00177 min^{-1}) on zeolite 3A, which suggested that the HF adsorption rate is faster than that of H_2S [6, 32].

(2) Diffusion Mechanism. The HF adsorption process on zeolite 3A can be divided into five continuous processes, as shown in Figure 11: (a) HF molecules diffuse from free state to adsorbent gas film (bulk diffusion), (b) HF molecules diffuse in the film (film diffusion), (c) HF molecules diffuse in pores between particles (interparticle diffusion), (d) HF molecules diffuse in 3A crystal (intraparticle diffusion), and (e) surface adsorption. Generally, surface adsorption and bulk diffusion are very fast, so they are ignored in the analysis of the HF adsorption kinetic process, and the role of the other three processes in the adsorption process is mainly considered.

(1) Film diffusion

Equations (11)–(14) can be used to predict HF adsorption control by particle or film diffusion [26, 27]. By plotting B_t vs. time, the mass transfer rate is controlled by pore diffusion if the plot is a straight line passing through the origin [26–28]. If the curve is nonlinear or does not pass through the origin, film diffusion can also be considered to affect the adsorption rate [26–28]. The calculated B_t values as a function of time are shown in Figure 12, and the curves

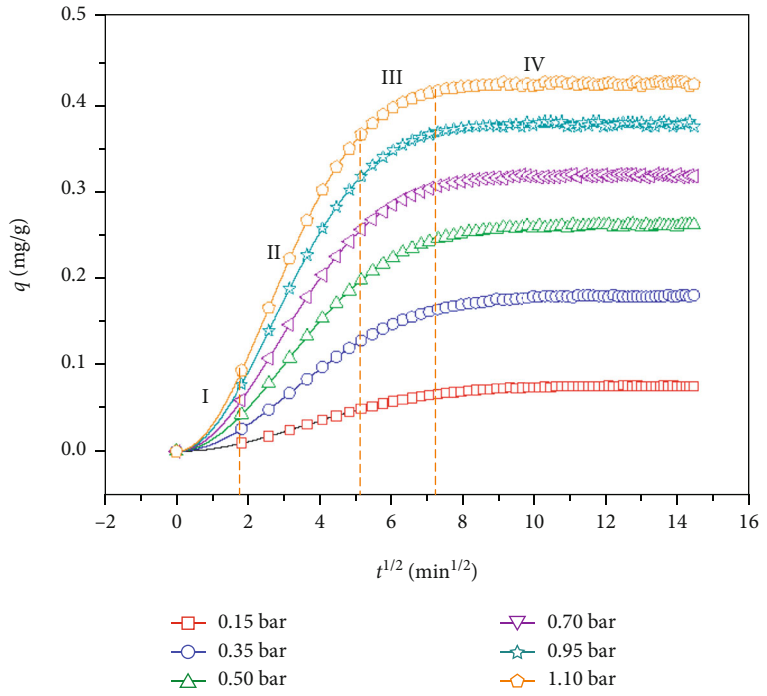

Figure 14: Prediction of intraparticle diffusion model for HF adsorption on 3A.

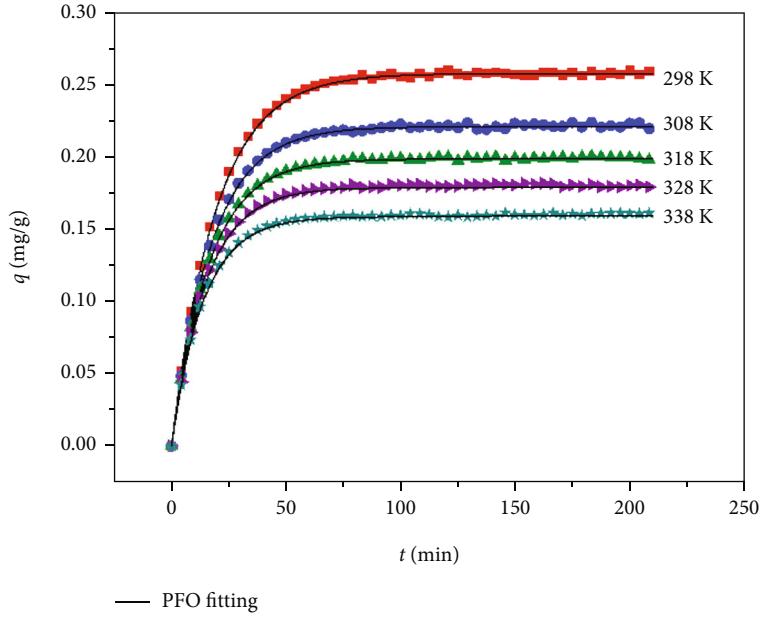

Figure 15: Dynamic curves of HF under different temperature at 0.5 bar.

are not entirely linear. The slopes and intercepts of the film diffusion model at all pressures are given in Table 3. The existence of intercept values suggests that the rate-controlling process for HF adsorption on zeolite 3A is mainly controlled by external mass transfer [26]. The intercept increases close to zero with increasing pressure, which indicates that pore diffusion appears to be more important at slightly higher pressures.

(2) Interparticle diffusion

The fitting results for the adsorption kinetics data with the interparticle diffusion linear form are shown in Figure 13 and Table 4. A good correlation between ln $[1 - q_t/q_e]$ with t indicates that the experimental data can be well described by the model. The D_c/r^2_p and D_c values calculated

Table 5: The fitting kinetic parameters for PFO and PSO.

Temperature (K)	Pseudo first-order			Pseudo second-order		
	q_1 (mg/g)	k_1	R^2	q_2 (mg/g)	k_2	R^2
298	0.2580	0.0534	0.9898	0.2832	0.2859	0.9685
308	0.2213	0.0592	0.9873	0.2411	0.3861	0.9726
318	0.1990	0.0633	0.9867	0.2157	0.4715	0.9724
328	0.1803	0.0681	0.9897	0.1944	0.5757	0.9675
338	0.1601	0.0733	0.9837	0.1718	0.7166	0.9523

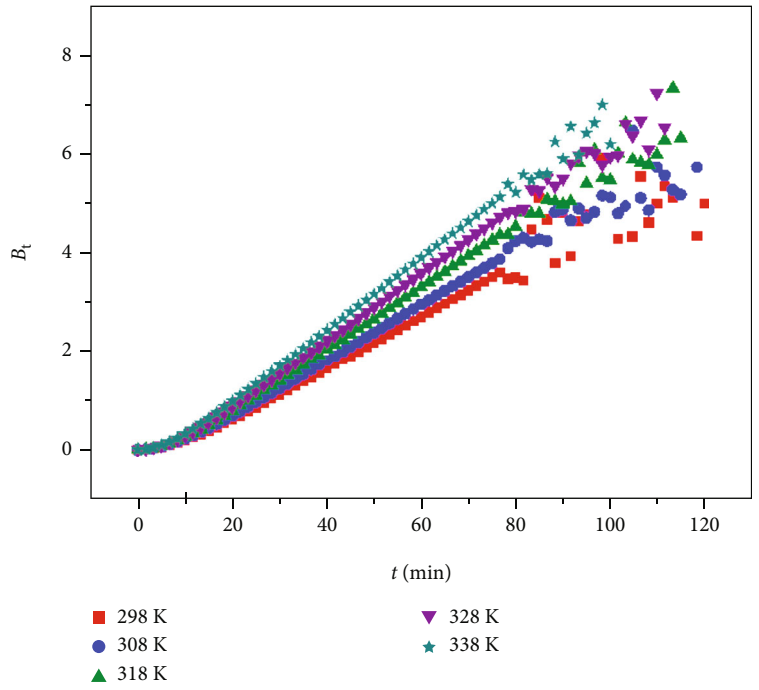

Figure 16: Plots of Boyd's film model for HF adsorption on 3A.

by the slope of the linear fit increase continuously with increasing pressure, indicating that high pressure favours the HF gas diffusion in zeolite 3A, which is consistent with the previous calculation that high pressure favours the adsorption rate. The order of magnitude of interparticle diffusion coefficient D_c of HF is 10^{-9} m^2/s. The intercept values obtained by linear fitting the experimental data are not close to −0.4977 (ln6/π^2), which indicates that the HF adsorption rate on zeolite 3A is not completely controlled by the interparticle diffusion. The calculated interparticle diffusion coefficient D_c/r^2_p versus first-order rate constant k_1 does not satisfy the 1/15 relationship and also reflects that the HF diffusion over zeolite 3A is not completely controlled by interparticle diffusion [26].

(3) Intraparticle diffusion

The intraparticle diffusion curves for HF adsorption on zeolite 3A are shown in Figure 14. The curves are observed to be nonlinear. According to the intraparticle diffusion model, the adsorption amount q_t plot vs. $t^{1/2}$ should be a straight line and pass through the origin of the mass transfer rate solely controlled by intraparticle diffusion [26]. Multilinearity can be observed when different processes are related to the adsorption mechanism. The slope of each linear portion represents the corresponding adsorption rate [27]. The curves in Figure 14 show quart-linear characteristics, indicating the presence of four consecutive HF adsorption steps on zeolite 3A. The initial part, region I, was ascribed to the HF diffusion from the free state to and through the gas film of zeolite 3A, and the initial stage was associated with the HF film diffusion. The second and third parts, regions II and III describe the adsorption-progressive stage where diffusion occurs within

Table 6: Kinetic parameters of linear fitting of film diffusion model.

Temperature (K)	Slope	Intercept	R^2
298	0.0526	−0.4048	0.9792
308	0.0583	−0.4042	0.9872
318	0.0623	−0.4054	0.9893
328	0.0670	−0.4044	0.9892
338	0.0721	−0.4032	0.9867

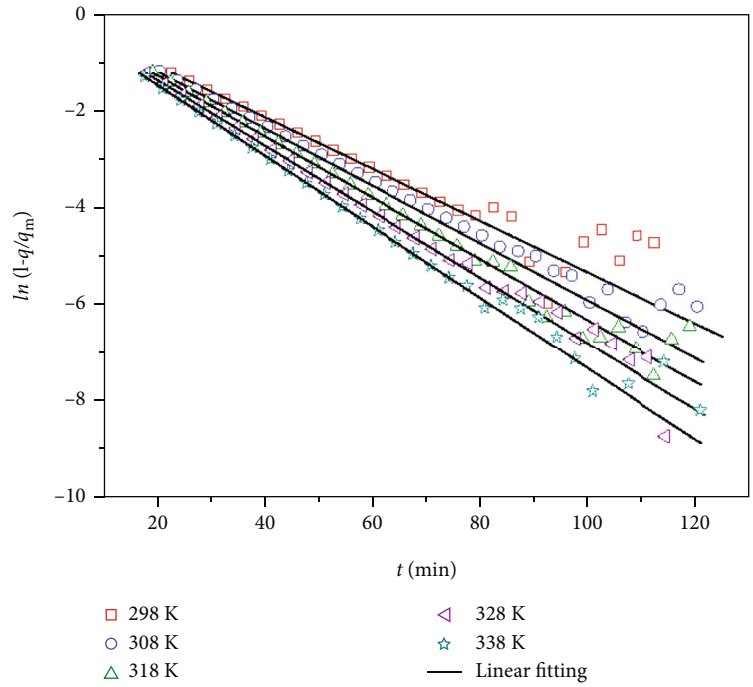

Figure 17: Linear fitting for experimental data with interparticle diffusion model.

the particle. Regions II and III are related to interparticle and intraparticle adsorptions, respectively. The fourth part, region IV, is the final equilibrium adsorption stage where the diffusion becomes slower owing to the active adsorption site saturation. Figure 14 shows that the extended line for straight lines corresponding to regions II and III does not pass through the origin, which may result from the different diffusion rates for the first and other stages of HF adsorption.

The adsorption rate of each HF molecule is controlled by four processes at a certain pressure. In the first stage, the adsorption rate is controlled by the film diffusion, as shown in segment I of Figure 14. The interparticle diffusion would be the rate-controlling process when the HF molecules diffuse into the particle pore. The intraparticle diffusion then controls the rate. Finally, the rate is governed by surface adsorption. The slope of each linear segment before region IV can be used to deduce which stage controls the whole HF adsorption rate [27]. Moreover, Figure 14 shows that the linear slope in region III is the smallest. The linear portion with the lowest slope is the rate-controlling step [27, 28]. This suggests that HF diffusion into the 3A particle is slower and the intraparticle diffusion stage is the rate-controlling stage. The linear slopes for regions II and III gradually increase with increasing pressure, which may be because the film thickness decreases as the pressure rises and the film diffusion rate will increase.

3.3.2. Effect of Temperature. Kinetic experiments at 298–338 K and 0.50 bar were conducted to investigate the effect of temperature on the HF kinetic adsorption on zeolites 3A. The HF adsorption kinetics curves at five temperatures are shown in Figure 15. The HF kinetic curves at five temperatures can be divided into three different stages: rapid adsorption, slow adsorption, and adsorption equilibrium stages. The HF adsorption capacity gradually decreases with increasing temperature, which is consistent with the discovery in literature [19]. High temperature enables the HF molecules to obtain more energy to overcome the intermolecular force and electrostatic interaction; thus, HF molecules remain in the free state. Simultaneously, the affinity between HF molecules and zeolite 3A surface will be weakened by the increasing temperature and will result in the decrease in adsorption capacity. In addition, high temperature is not conducive to the formation of a more orderly and stable configuration of adsorbed molecules, resulting in the reduction of adsorption capacity. Higher temperature is not conducive to improving HF adsorption recovery. It can also be found that the time to reach equilibrium decreases with the increasing temperature, which also shows that the temperature is conducive to the gas adsorption rate.

Table 7: The linear fitting results for interparticle diffusion model.

Temperature (K)	Slope	Intercept	D_c/r^2_p (10^{-3} s^{-1})	D_c (10^{-9} s^{-1})
298	−0.0534	0.00001	5.416	1.354
308	−0.0592	−0.00003	6.004	1.501
318	−0.0633	0.00008	6.420	1.605
328	−0.0681	−0.00001	6.907	1.727
338	−0.0733	0.00001	7.434	1.859

(1) Adsorption Rate. The PFO and PSO models were used to predict the HF adsorption kinetic curves. The fitting results are shown in Figure 15 and Table 5. The adsorption rate constants k_1 and k_2 of HF increase with temperature,

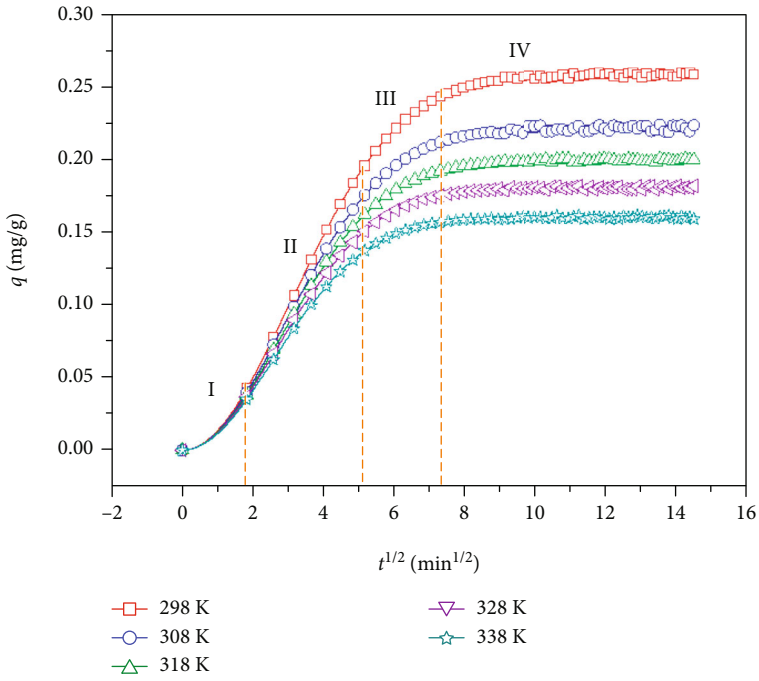

Figure 18: Prediction of intraparticle diffusion model for HF adsorption on 3A.

indicating that the HF adsorption rate shows a positive correlation with temperature, which is due to the acceleration of molecular motion caused by temperature increase. q_1 and q_2 decrease with increasing temperature, suggesting that higher temperature is conducive to gas diffusion; however, it will reduce the gas adsorption capacity.

(2) Diffusion Mechanism.

(1) Film diffusion

The calculated B_t values are shown in Figure 16. Moreover, B_t is not completely linear. The slope and intercept of Boyd's film diffusion model are listed in Table 6. The existence of intercept value shows that the HF adsorption rate on zeolite 3A was mainly controlled by external mass transfer. The intercept values decrease slightly with increasing temperature, suggesting that pore diffusion become more important at high temperature. The B_t values show a positive correlation with temperature, indicating that the film diffusion rate increases with temperature increase.

(2) Interparticle diffusion

The linear fitting results for the HF adsorption kinetic curve using the interparticle diffusion model at five temperatures and 0.5 bar are shown in Figure 17 and Table 7. A good correlation between $\ln [1 - q_t/q_e]$ shows that t indicates that the experimental data can be well described by the model. In addition, Table 7 shows that D_c/r^2_p and D_c values increase with increasing temperature. Based on molecular dynamics theory, the essence of HF diffusion in zeolite 3A is due to the molecular irregular thermal movement. The average kinetic energy of HF molecules increases with temperature, which leads to an increase in amplitude and frequency of molecular vibration. The higher molecular irregular thermal movement intensity occurs at a higher temperature. Consequently, the HF diffusion rate in zeolite 3A becomes faster.

(3) Intraparticle diffusion

The quart-linear characteristics for intraparticle diffusion curves can be observed in Figure 18, which indicated that three different processes are involved in the adsorption mechanism. The curves of the five temperatures in the first stage I are relatively close, indicating that the influence of temperature on the HF diffusion velocity from the free state to and through the gas film of zeolite 3A is little. In the second and third stages, the difference between the five curves increases with time. The linear slope for each stage decreases with increasing temperature, suggesting that the pore diffusion rate in the particles decreases slightly at this stage, which may be due to the impediment of diffusion by the interaction of HF molecules under high pressure. The same trend is also found in CO_2 in porous MgO [27]. The extended line for straight lines corresponding to regions II and III does not pass through the origin. The linear portion for stage III with the lowest slope indicates that the diffusion rate is controlled by intraparticle diffusion.

4. Conclusion

HF adsorption isotherms data on zeolite 3A at 298–338 K were type I. The adsorption capacity increased with

increasing pressure and decreases with increasing temperature. HF adsorption isotherms data on zeolite 3A can be described well by the DA model. The H_{st} values of HF on zeolite 3A decreased with the increase of surface load, which suggested the surface energy heterogeneity of zeolite 3A.

The HF adsorption by zeolite 3A at different adsorption conditions followed simple first-order kinetics. The first-order rate increased with pressure and temperature. The calculated B_t values showed nonlinear characteristics with time. B_t values increased with increasing pressure and temperature, indicating that high pressure and temperature favour film diffusion. The order of magnitude of the interparticle diffusion coefficient D_c of HF on zeolite 3A was $10^{-9}\,m^2/s$. The higher pressure and higher temperature favour the HF diffusion process. The intraparticle diffusion curves for HF adsorption on zeolite 3A showed quart-linear characteristics, indicating the presence of three consecutive HF adsorption steps on zeolite 3A. In the initial adsorption stage, the film diffusion controlled the adsorption rate. The intraparticle diffusion would be the rate-controlling process after HF molecules diffuse through the film. The intraparticle diffusion then controls the rate. Finally, the rate was governed by surface adsorption. HF diffusion into the particle of zeolite 3A was the slowest and therefore, the intraparticle diffusion is the rate-controlling stage.

In this study, the HF adsorption mechanism onto zeolite 3A was evaluated based on kinetics and thermodynamics. However, only one adsorbent zeolite 3A was studied due to limited conditions, and other porous materials have not been analyzed in this paper. The adsorption kinetics and thermodynamics of HF on different materials will be compared in subsequent studies.

Data Availability

All data included in this study are available upon request by contact with the corresponding author.

Conflicts of Interest

The authors declare that they have no conflicts of interest.

Acknowledgments

This work was supported by the Project of the State Key Laboratory of Laser Interaction with Matter (SKLLIM1813), Natural Science Foundation of Hebei Province (E2020402072), and The Handan Science and Technology Research and development projects (19422091008-31).

References

[1] P. Kumar, S. Suganya, S. Srinivas, S. Priyadharshini, and E. Lichtfouse, "Treatment of fluoride-contaminated water: a review," *Environmental Chemistry Letters*, vol. 17, no. 4, pp. 1707–1726, 2019.

[2] J. Wang, S. Deng, R. Zhao, and L. Zhao, "Analysis of energy and consumption reduction in adsorption recovery of electronic HF," *Chemical Industry and Engineering Progress*, vol. 40, pp. 3645–3655, 2021.

[3] S. Zhou, L. Ma, K. Huang et al., "Purify technology of laser medium in non-chain pulsed HF laser," *Acta Photonica Sinica*, vol. 45, no. 3, article 314004, 2016.

[4] J. Lucsa, F. Smektala, and J. L. Adam, "Fluorine in optics," *Journal of Fluorine Chemistry*, vol. 114, no. 2, pp. 113–118, 2002.

[5] C. B. Mcpake and G. Sandford, "Selective continuous flow processes using fluorine gas," *Organic Process Research Development*, vol. 16, no. 5, pp. 844–851, 2012.

[6] A. Starke, C. Pasel, C. Bläker, T. Eckardt, J. Zimmermann, and D. Bathen, "Impact of Na^+ and Ca^{2+} cations on the adsorption of H_2S on binder-free LTA zeolites," *Adsorption Science and Technology*, vol. 2021, article 5531974, 12 pages, 2021.

[7] Z. Jing and X. Ying, "Adsorption and recovery technology of excess hydrogen fluoride in the production of fluorine-containing chemicals," *Organo-Fluorine Industry*, vol. 3, 2007.

[8] J. Luo, S. Wang, and X. Yang, "Progress in the techniques and applications of dealing with hydrogenl fluoride," *New Chemical Materials*, vol. 39, pp. 33–36, 2011.

[9] C. Li, S. He, D. Jiang, and Q. Li, "Hydrogen fluoride adsorption ability of some inorganic compounds," *Advanced Materials Research*, vol. 412, pp. 1–4, 2011.

[10] H. Tavakoli and M. Ghasemi, "Equilibrium, kinetics and breakthrough studies for adsorption of hydrogen fluoride on sodium fluoride," *Chemical Engineering and Processing*, vol. 49, no. 4, pp. 435–440, 2010.

[11] S. Afzal, A. Rahimi, M. Ehsani, and H. Tavakoli, "Experimental study of hydrogen fluoride adsorption on sodium fluoride," *Journal of Industrial and Engineering Chemistry*, vol. 16, no. 1, pp. 147–151, 2010.

[12] S. Afzal, A. Rahimi, M. Ehsani, and H. Tavakoli, "Modeling hydrogen fluoride adsorption by sodium fluoride," *Journal of Industrial and Engineering Chemistry*, vol. 16, no. 6, pp. 978–985, 2010.

[13] T. Liu, S. Wang, and L. Dong, "The optimal technique parameter mensuration of sodium fluoride adsorb hydrogen fluoride," *Ship Science and Technology*, vol. 31, pp. 109–111, 2009.

[14] K. Wu, "Adsorption characteristics of hydrogen fluoride on alumina," *Environmental Pollution Control*, vol. 12, pp. 34–36, 1990.

[15] J. Sheng, *Theoretical and Experimental Study on Dry Adsorption of HF Gas*, Zhejiang University, Zhejiang, China, 2004.

[16] D. Che, G. Xu, and S. Xu, "Studies on adsorption properties of DB18C6/SiO2 Composite material toward Zr (IV) AND Hf (IV)," *Mining Metallurgy*, vol. 24, pp. 35–40, 2015.

[17] M. A. Siahooei and K. Bordbari, *Adsorption of Fluoride Gases in Aluminum Production by Using of Nanotechnology*, Springer International Publishing, Berlin, 2019.

[18] C. Wang, B. Liu, F. Sun, J. Xie, and Q. Pan, "New challenge of microporous metal-organic frameworks for adsorption of hydrogen fluoride gas," *Materials Letters*, vol. 197, pp. 175–179, 2017.

[19] H. Bahrami, J. Safdari, M. A. Moosavian, and M. Torab-Mostaedi, "Adsorption of hydrogen fluoride onto activated carbon under vacuum conditions: equilibrium, kinetic and thermodynamic investigations," *Chemical Industry and Chemical Engineering Quarterly*, vol. 18, no. 4-1, pp. 497–508, 2012.

[20] J. A. D. Dobladez, V. I. Á. Maté, S. Á. Torrellas, M. Larriba, G. P. Muñoz, and R. A. Sánchez, "Comparative simulation study of methanol production by CO_2 hydrogenation with 3A, 4A and 5A zeolites as adsorbents in a PSA reactor,"

Separation and Purification Technology, vol. 262, article 118292, 2021.

[21] R. D. Mccarty and V. D. Arp, "A new wide range equation of state for helium," *Advances in Cryogenic Engineering*, vol. 35, pp. 1465–1475, 1990.

[22] D. D. Duong, *Adsorption Analysis: Equilibria and Kinetics*, Imperial College Press, London, 1998.

[23] C. L. Yaws and M. A. Satyro, *The Yaws Handbook of Vapor Pressure (Second Edition)*, Gulf Professional Publishing, 2015.

[24] S. Duan, M. Gu, M. Tao, and K. Huang, "Adsorption characteristics and thermodynamic property fields of methane and Sichuan Basin shales," *Adsorption*, vol. 28, no. 1-2, pp. 41–54, 2022.

[25] S. Rodríguez-Narciso, J. Lozano-Álvarez, R. Salinas-Gutiérrez, and N. Castañeda-Leyva, "A stochastic model for adsorption kinetics," *Adsorption Science and Technology*, vol. 2021, article 5522581, 21 pages, 2021.

[26] S. Loganathan, M. Tikmani, S. Edubilli, A. Mishra, and A. Ghoshal, "CO_2 adsorption kinetics on mesoporous silica under wide range of pressure and temperature," *Chemical Engineering Journal*, vol. 256, pp. 1–8, 2014.

[27] G. Song, X. Zhu, R. Chen, Q. Liao, Y. Ding, and L. Chen, "An investigation of CO_2 adsorption kinetics on porous magnesium oxide," *Chemical Engineering Journal*, vol. 283, pp. 175–183, 2016.

[28] S. Basu, G. Ghosh, and S. Saha, "Adsorption characteristics of phosphoric acid induced activation of bio- carbon: equilibrium, kinetics, thermodynamics and batch adsorber design," *Process Safety and Environmental Protection*, vol. 117, pp. 125–142, 2018.

[29] K. L. Tan and B. H. Hameed, "Insight into the adsorption kinetics models for the removal of contaminants from aqueous solutions," *Journal of the Taiwan Institute of Chemical Engineers*, vol. 74, pp. 25–48, 2017.

[30] Y. Wang, "Measurements and modeling of water adsorption isotherms of zeolite linde-type A crystals," *Industrial & Engineering Chemistry Research*, vol. 59, no. 17, pp. 8304–8314, 2020.

[31] J. Cao, P. Wang, and Q. Sun, "Green synthesis of magnetic zeolite LTA using NaOH activated fly ash," *Zeitschrift fitsanorganische und allgemeine Chemie*, vol. 646, no. 20, pp. 1666–1670, 2020.

[32] A. G. Georgiadis, N. D. Charisiou, S. Gaber, K. Polychronopoulou, and M. A. Goula, "Adsorption of hydrogen sulfide at low temperatures using an industrial molecular sieve: an experimental and theoretical study," *ACS Omega*, vol. 6, no. 23, pp. 14774–14787, 2021.